

This is the preprint of the contribution published as:

Birnstengel, S., Dietrich, P., Peisker, K., Pohle, M., Hornbruch, G., Bauer, S., Hu, L., Günther, T., Hellwig, O., Dahmke, A., **Werban, U.** (2024):

Experimental seismic crosshole setup to investigate the application of rock physical models at the field scale

Geophysics **89** (3), MR183 - MR195

This work was supported by the Bundesministerium für Bildung and Forschung (BMBF) within the funding initiative “Forschung für Nachhaltige Entwicklung (FONA3)”, Project TestUM-Aquifer (Grant 03G0875B).

The publisher's version is available at:

<https://doi.org/10.1190/geo2022-0625.1>

Experimental seismic crosshole set up to investigate the application of rock physical models at the field scale

Susann Birnstengel¹, Peter Dietrich¹, Kilian Peisker¹, Marco Pohle¹, Götz Hornbruch², Sebastian Bauer², Linwei Hu², Thomas Günther³, Olaf Hellwig⁴, Andreas Dahmke², Ulrike Werban¹

¹Department of Monitoring- and Exploration Technologies, Helmholtz Centre for Environmental Research, Permoserstraße 15, 04318 Leipzig, Germany

²Department of Geosciences, Christian Albrechts Universität zu Kiel, Christian Albrechts Platz 4, 24118 Kiel, Germany

³Leibnitz Institute for Applied Geophysics (LIAG), Stillweg 2, 30655 Hannover, Germany

⁴Faculty of Geoscience, Geoengineering and Mining, TU Bergakademie Freiberg, Gustav-Zeuner-Str. 12, 09599 Freiberg, Germany

ABSTRACT

Seismic crosshole techniques are powerful tools to characterize the properties of near-surface aquifers. The knowledge of rock-physical relations at the field scale is essential for interpreting geophysical measurements. Though it remains difficult to up-scale the results of existing laboratory studies to the field due to the usage of different frequency ranges. To address this, we developed an experimental layout which was successfully applied for surveying the dependency of gas saturation on seismic properties. The integration of geophysical measurements into a hydrogeological research question allows us to prove the applicability of theoretical rock physical concepts at the field scale. It sets a scarce link to the discipline of hydrogeophysics. We used

crosshole seismics to perform a time lapse study on a gas injection experiment. With a controlled CH_4 injection at 17.5 m depth we achieved a guided alteration in sediments water saturation and monitored the process of saturation change in a time lapse experiment for a period of twelve months covering an observational depth of 8-13 m. The investigation contained a prior P-wave simulation followed by a data-based P-wave velocity analysis. A subsequent comparison of our seismic data with in-situ water content measurements using different approaches shows reasonable compliance and approves the method for gas leakage detection. We demonstrate that our seismic crosshole setup is able to verify rock physical relations at the field scale and additionally quantify relative water content changes in the subsurface.

INTRODUCTION

As part of energy transition research, the expanded supply and distribution infrastructure faces the challenge of gas leakages and entries at the near surface. The assessment and monitoring of gas storage and distribution facilities, together with corresponding induced processes in the near surface is crucial but not restricted to a reliable risk assessment and impact analysis on our groundwater resource. With geophysical methods it is possible to detect, determine and validate the dynamics of subsurface parameters such as porosity, saturation and permeability and hence conduce to the observation of hydrogeological processes in the subsurface (Jorgensen, 1989; Diallo, 2000; Lamert et al., 2012). The recognition of integrating geophysical measurements into hydrogeological studies grows and could significantly advance our understanding of dynamic hydrogeological processes, especially at intermediate scale (m) (Robinson et al., 2008). Hydrogeophysical investigations sharpen the fo-

cus on an improved understanding of hydrogeological processes through geophysical observations in particular. Since those observations do not generally provide direct information about hydrogeological properties, their effective use is governed by the strength of the relationships between estimated geophysical properties and the properties of interest (Binley et al., 2015; Blazevic et al., 2020). Therefore, finding and evaluating a reliable relationship between rock and geophysical parameters is important as they are individually subjected to natural environmental and anthropogenous influences.

Geophysical monitoring and seismic surveys for gas detecting technologies (Lumley et al., 2008; Pevzner, 2020; Trautz, 2020) as well as geotechnical site investigation (Hing Ng et al., 2019) or time-lapse studies with multi-method approaches (Dangeard et al., 2021) have been applied, discussed and improved over time. Borehole techniques like vertical seismic profiling (VSP) or crosshole tests, including tomography, although still sparsely used, are applicable to monitor gas injections and variances in reservoir conditions (Hing Ng et al., 2019). Crosshole tests provide a depth profile of P- and S-wave velocities. The procedures are outlined in ASTM test designation D4428 M-84 (1984). There are various examples of the application of seismic methods in the exploration of carbon capture and storage sites, e.g., to detect the change in seismic velocity and to image the gas distribution in the reservoir (Zhang et al., 2012; Götz, 2014; Onishi et al., 2009) or even model CO_2 saturation (Hu et al., 2017). A crosshole seismic layout modification by Diallo (2000) enables an interpretation independent from the source signal whilst being decoupled from surface noise. Especially,

the seismic P-wave velocity is greatly affected by the water content in unconsolidated materials (Allen et al., 1980), and the signal is hence sensitive to changes in the fluid component. Note that the position of the groundwater table strongly influences the P-wave. Its application for deriving geotechnical parameters is limited (Paasche et al., 2009). Whereas capillary pressure strongly affects both P- and S- waves (Solazzi et al., 2020; Romero-Ruiz et al., 2021), shear waves react sensitively to changes in dynamic soil parameters, such as shear strength or modulus of elasticity (Dietrich and Tronicke, 2009). Geistlinger and Zulfiqar (2020) studied the influence of wettability and surface roughness on fluid displacement in detail, whereas we simplify that the injected gas displaces the fluid phase. This results in material compressibility changes through the alteration of the bulk modulus (Nanda, 2016), affecting the signal amplitude. Thus, seismic velocity and amplitude are excellent proxies to image gas induced parameter changes. One key challenge is the limitation of the measurement scale and its resolution. The characterized target may be much smaller than the footprint of the geophysical measurement (Binley et al., 2015). Financial limitations of invasive in-situ sampling of the subsurface enforce interpretation based on a few observations at shallow depths. Knowing that the subsurface process or property under investigation can be scale-dependent (e.g. Schulze-Makuch et al. (1999)), those measurements are limited by the scale they offer (Binley et al., 2015).

Our goal is to determine and, in a first attempt, to quantify rock-physical dependencies by influencing the fluid component with methane gas in a controlled manner. In this paper, we describe and discuss a methane gas injection experiment and its

monitoring at the field scale at the test site "TestUM" in Wittstock/Germany. We investigate the ability of a near-surface seismic crosshole setup to resolve petrophysical parameter changes and test the repeatability of our experimental design for time-lapse interpretation. The focus lies on the data analysis to extract the seismic velocity that is discussed in the matter of indicating and quantifying changes in the pore fluid. Due to the size of our local borehole installations, we concentrate our investigation on seismic P-waves. In the saturated zone, its propagation velocity is governed by the pore fluid and not the formation density (Wightman et al., 2004). In order to avoid 2D and 3D effects in space, we perform a time-lapse borehole experiment. We compare the results relative to each other before we finally match them with our water content measurements. Analyzing the data regarding rock-physical interpretation is essential to debate its applicability for gas leakage detection. By reviewing Gassmann's equation, using the approach of Mavko et al. (1995) to solve them without knowing S-wave velocity and the time-average relation when considering a "patchy saturation", we discuss different approaches to calculate the gas content in the subsurface. We aim to analyze and interpret a hydrogeophysical field study using rock physical relations.

TEST SITE

The test site, located in the north of Germany close to Wittstock/Dosse (N 53° 11' 38.9616, E 12° 30' 11.178; Figure 1A), has partly been used for a CO_2 storage experiment in 2010 (Peter et al., 2012), and a heat storage experiment being part of the "TestUM" project that started in 2019 (Keller et al., 2021; Lüders et al., 2021; Heldt et al., 2021). Combining geophysical and in-situ hydrogeological exploration

techniques results in a comprehensive picture of the geological and hydrogeological subsurface properties. We first applied a spacious electromagnetic survey across the whole test site to detect metal scrapes and old wiring in the upper 6 m and thus to assure drilling clearance in the whole area. In addition, six electrical resistivity tomography (ERT) profiles between 110 and 270 m length across the test site provided initial stratigraphical information of the upper 20 m (Hausmann et al., 2013; Lamert et al., 2012; Peter et al., 2012). As a third step, we combined this information with the in situ hydraulic characterization in selected areas using direct push (DP) technologies (Dietrich and Leven, 2006; Köber et al., 2009). Measurements with the hydraulic profiling tool (HPT) (Dietrich et al., 2008) and the electrical conductivity (EC) log resulting in a depth-orientated stratigraphical interpretation. Figure 1C shows a drop of the relative hydraulic conductivity at 9 m depth that indicates a low permeable layer corresponding with slightly higher electrical conductivity values. Additional slug tests (Butler, 1997) and sediment core samples validate the hydrogeological and support the geological evaluation (Figure 1C, D). The sediment core showed coarse-grained sand on top followed by a clay layer and a subsequent fine-grained sand with a bulk density of 1610 kg/m^3 intermittent by clay and silt with a bulk density of 1720 kg/m^3 according to laboratory measurement. Nuclear magnetic resonance (NMR) measurements (Dlugosch, 2014) at the test site showed a porosity of 35.3 % in RB1 at 11 m depth. We attained an informative picture on sediment parameters at a local scale and identified a suitable test site for our methane gas injection experiment. Appendix E offers information about the test site labeling and the data set availability.

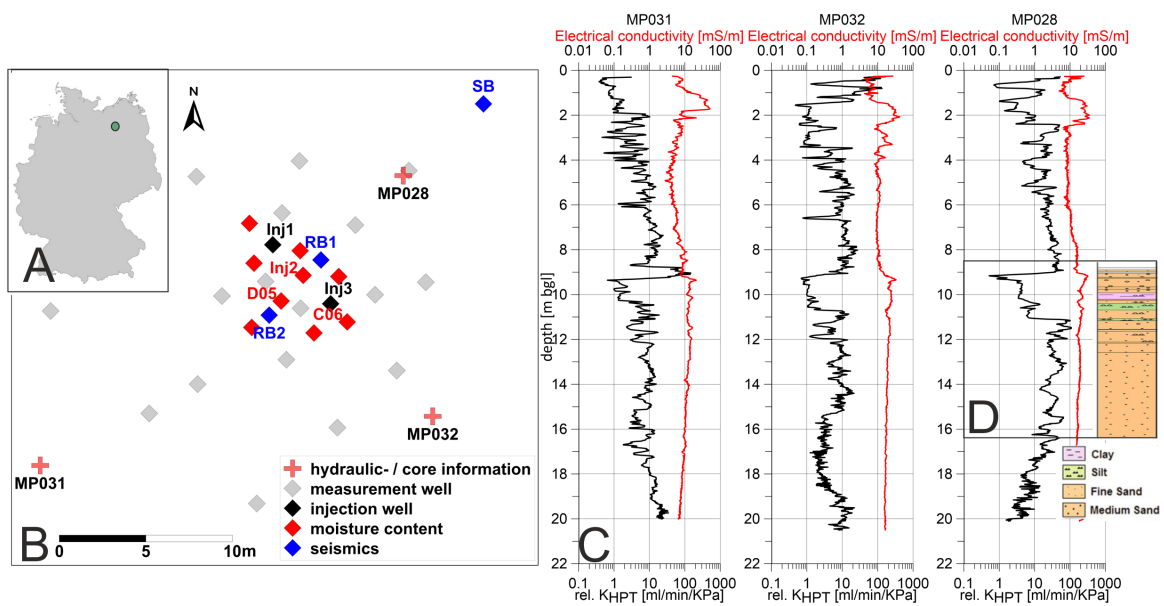


Figure 1: (A) Location of test site for CH_4 injection and (B) Experimental layout for CH_4 injection with different types of measuring wells. (C) Three hydraulic (black) and electrical conductivity (red) profiles at $MP32$, $MP31$, $MP28$ measured with the Hydraulic Profiling Tool (HPT) and (D) core profile of $MP28$ from 8-16 m depth.

METHODOLOGY

Experimental Design

We tested saturation dispersion models of the methane injection on several injection strategies for our particular geological setting. They predicted a plume forming upwards migration of the gas phase with an accumulation right beneath the low-permeable loam at 9 m depth (Dahmke et al., 2021). For hydrogeochemical and hydrogeological reasons, we want to assure a long duration of upwards gas migration. Hence, we benefit from a long observational period before the gas accumulates beneath the permeable loam or degasses to the surface. Therefore, we preferred the lowermost possible gas injection at 17.5 m depth. The methane gas injection experiment (Figure 1B) consists of three central injection lances with an injection depth of 17.5 m, taking advantage of the homogeneity of the second aquifer sediment. Three 2" boreholes of high-density polyethylene (HDPE) are located transverse to the injection lances and inline to each other up to a depth of 17 m for seismic crosshole measurements (Figure 1B). Additional soil water content information is provided at eight adjacent wells together with the injection wells at 11 m, 14 m and 17 m depth using 22 moisture sensors (SMT-100, Truebner) in total (Figure 1B). An amount of 35 kg gaseous CH_4 was injected over a period of two days with an over-pressure of 3.5 bar to stand against water pressure in depth and took place from May 14 to May 16, 2019. Our seismic data acquisition comprised the baseline measurements on April 29, 2019 and seven monitoring cycles starting on May 21, 2019 (Table 1). To avoid the influence of gas-induced seismicity, our monitoring started five days after injection.

Table 1: Monitoring period

Date	Days after injection	Measurement
April 29, 2019		Baseline Monitoring
May 14-16, 2019		Injection
May 21, 2019	5	Monitoring
June 3, 2019	18	Monitoring
July 4, 2019	49	Monitoring
January 22, 2020	251	Monitoring
February 17, 2020	276	Monitoring
March 5, 2020	287	Monitoring
May 5, 2020	355	Monitoring

Seismic crosshole experiment

In crosshole seismic experiments, we measure traveltime and derive velocity of seismic waves between boreholes. We make use of the conventional approach, which resembles horizontal transmission. Source and receiver are located at the same depth, analogical to a tomographic setup. The shot is recorded at each depth and analyzed for horizontal transmission. That enables us to monitor controlled subsurface variations in a delimited area. We installed a source borehole (SB) and two receiver boreholes ($RB1$, $RB2$) inline. The gas injection takes place between $RB1$ and $RB2$ (Figure 1B). The small distance of 4.4 m between $RB1$ and $RB2$ allows the area to change the saturation parameter distinctly while being filled with gas. SB is situated at a larger distance of 13 m to $RB1$ and 17.4 m to $RB2$. We focus our measurements on the upper area between 8-13 m depth based on the preconditioned models of gas migration (Dahmke et al., 2021). SB was equipped with a borehole sparker SBS42 generating a highly repeatable signal provided by an impulse generator IPG5000 that operates at 5 kV for high voltage power supply, manufactured by Geotomographie GmbH, Germany. Two hydrophone strings (BHC4, Geotomographie (2021)), one with 17, and one with 24 hydrophones of small diameter, were mounted into $RB1$ and $RB2$ accordingly from 8-13 m depth with a hydrophone spacing of 1 m. The

first set of 10 shots was released at 13 m depth and the sparker was pulled up with a shot increment of 1 m (Figure 2). In both receiver boreholes, we recorded and stacked ten shots for each depth during the baseline measurement and every monitoring cycle to increase the signal-to-noise ratio. Our sampling interval was $20.833 \mu\text{s}$, and the recording covered 30 ms. Source and receivers were acting below the groundwater table for coupling reasons. The wells' siltation process restricted our operational depth to 13 m. In order to obtain comparable data for time-series measurements, and assure data quality and repeatability, all baseline and monitoring measurements have been repeated throughout their whole execution. We conducted a complete dismantling and re-installation of the seismic crosshole setup to ensure reliable detection at the hydrophones and to exclude manual handling errors throughout the measuring process. The raw data consists of a total number of 48 traces per monitoring stage for six different depths. We resorted the data to account for horizontal transmission. At every depth, we are looking at six different traces per receiver borehole. The corresponding figure is available in Appendix A.

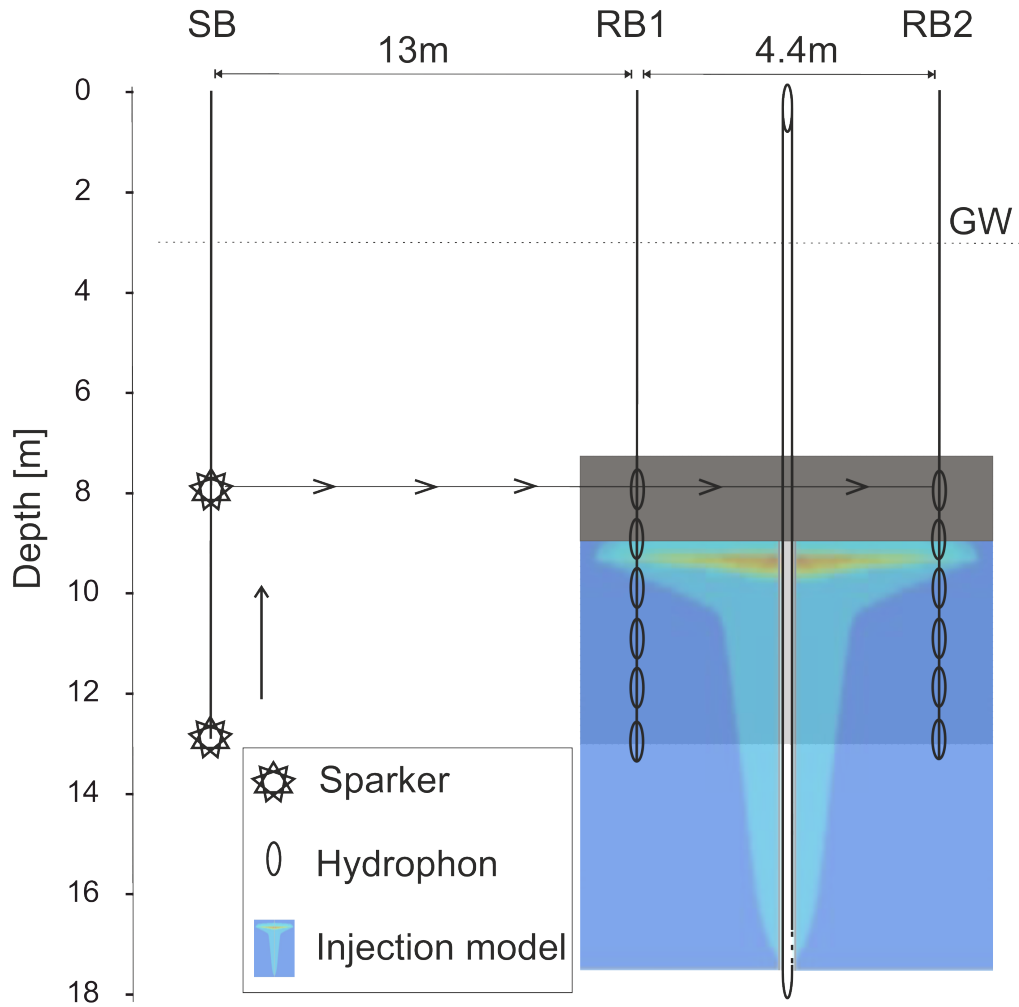


Figure 2: Three HDPE wells (CMT-System, Solinst) are installed inline. The P-wave sparker in *SB* operates at a depth from 13 to 8 m depth. The hydrophone strings in *RB1* and *RB2* cover the same depth range. The groundwater table is located at 3 m depth. The gas is injected between *RB1* and *RB2* at a depth of 17.5 m via three injection lances. The injection model shows a possible saturation dispersion scenario with the highest gas phase saturation accumulating beneath the low permeable loam.

2D seismic wave simulation

For the feasibility assessment prior to our experiment, we need to comprehend the seismic wave behaviour in the subsurface and its changes during fluid variations. To simulate the propagation of seismic waves in and around boreholes, we applied a 2D finite-difference time domain program FDBH (Finite Difference BoreHole), originally developed by Thomas Bohlen and described by Randall et al. (1991). We apply a version that is based on the velocity-stress formulation of the seismic wave equation (Hellwig, 2017). The model parameters have been estimated after tabular values (Schön, 2015; Meister, 2012), and our baseline measurements. The gas-water saturated sand indicates the gas injection.

Model dimension:

Table 2 gives an overview of the model dimension. To avoid numerical dispersion during the simulation the grid spacing was set on 500 cells with a spacing of 0.002 m. The size of the finite difference (FD)-grid enfolds 30 m x 15 m which corresponds to 15000 x 7500 grid cells. The model top is described by a free surface boundary, whereas the bottom and side boundary are described by perfectly matched layers to account for wave absorption. The frequency of the source signal (Ricker signal, Appendix B) is set to 5 kHz, providing a main frequency of 4.3 kHz. It originates from manufacture's data.

Table 2: Model dimension. Source pressure rate is first deviation after time of a bell curve with the main frequency of 4.8 kHz.

	x [m]	z [m]
Dimension	-5 - 25	0 - 15
Source	0	8 - 13
Receiver	13 / 17.4	8 - 13
Sampling interval [ms]	0.0008	
Sampling interval [mm]	0.02	
Record time [ms]	25	
Time steps	31250	
Samples (seismogram)	1250	

Model parameter:

The model parameters in Figure 3 show the water saturated and gas-water saturated case.

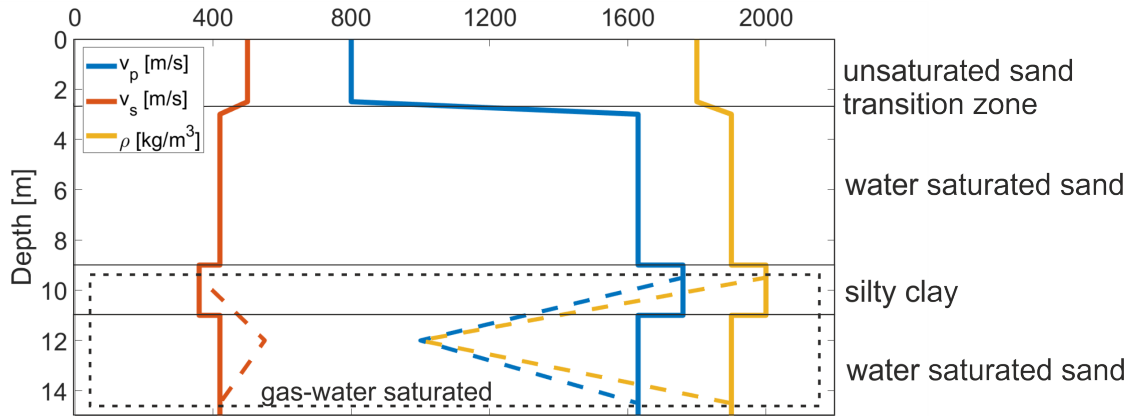


Figure 3: Overview of the applied model parameters. At 2.5 m - 3.0 m depth the transition zone marks the groundwater table represented by linear saturation interpolation. The solid line marks the fully water saturated case, the dashed line marks the gas-water saturated case. A radial gas concentration decrease is implemented to 5 m lateral extent, center at $x = 14.5$ m and $z = 12$ m depth with maximum gas concentration.

Figure 4 shows the elastic wavefield while shooting at 8 m depth. The reflection on the silty clay (low permeable) boundary and the groundwater surface is visible. The wave travels faster through the low permeable layer. A refracted wave is visible at 0.01 s in front of the second hydrophone chain at 11 m depth. On the right side of Figure 4, we can clearly see the gas influence on the waves' travel time below the low permeable

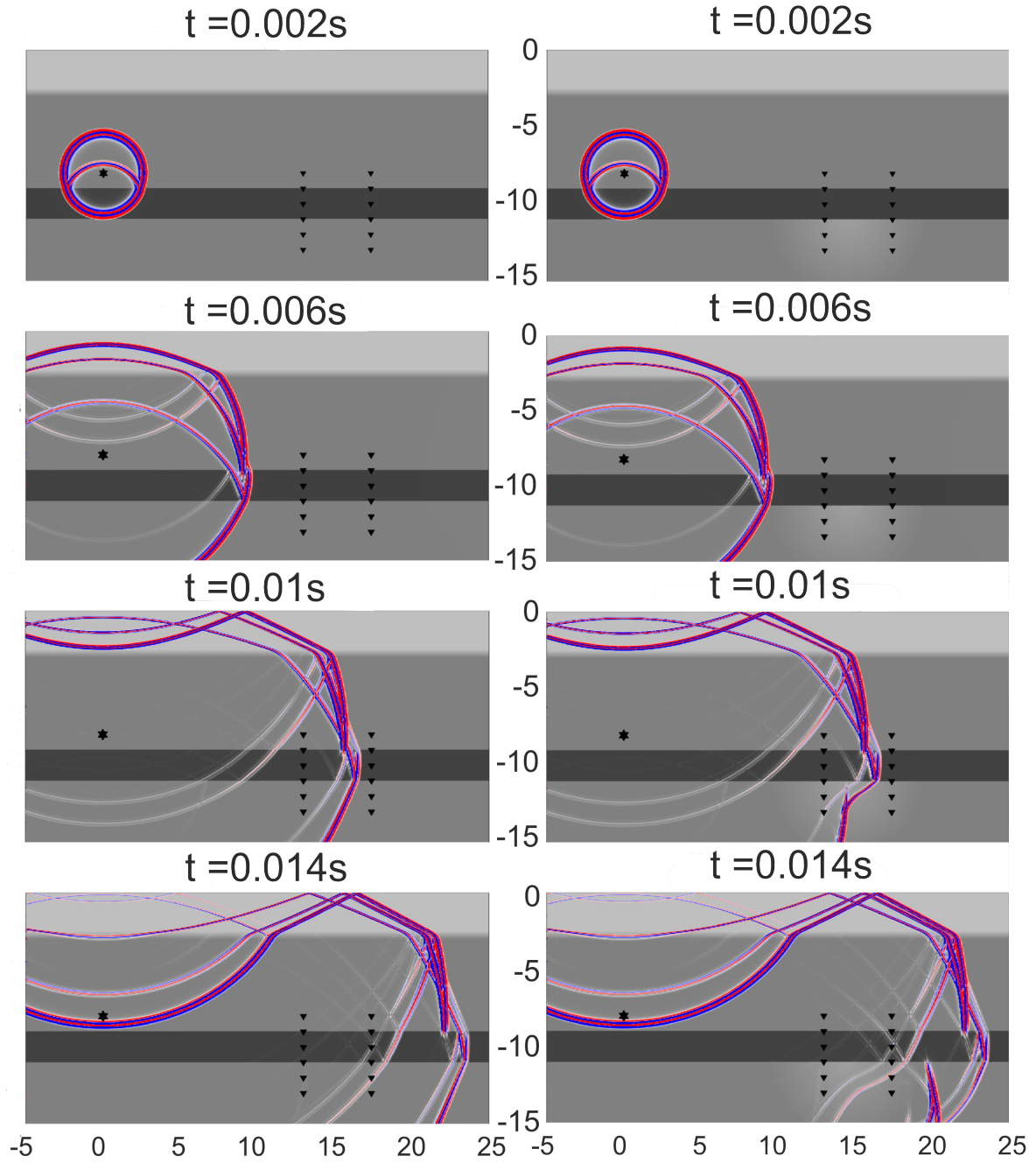


Figure 4: Simulated P-wave travel path for shot at 8m depth without gas (left) and with gas lens center at $x = 14.5$ m and $z = 12$ m depth (right)

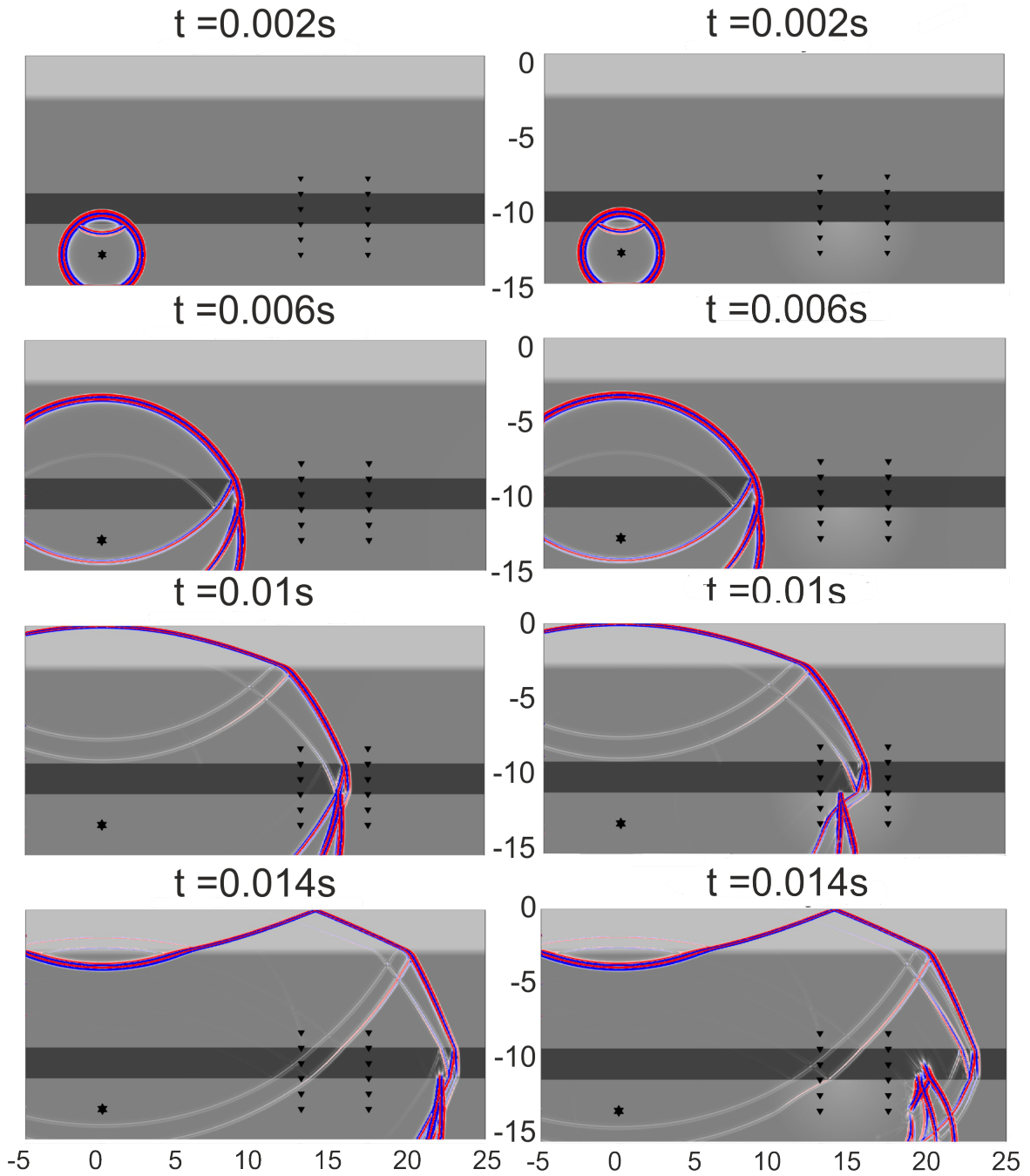


Figure 5: Simulated P-wave travel path for shot at 13 m depth without gas (left) and with gas lens center at $x = 14.5$ m and $z = 12$ m depth (right)

layer. In Figure 5, the P-wave simulation in 13 m depth, refraction and reflections, also within the low permeable layer, are occurring. We see less influence from surface reflections. Refracted waves along the boundary between the low permeable layer and the sandy aquifer become obvious. Therefore, we consider conducting a time-lapse study, where comparisons between the baseline and the monitoring cycle account for changes in the subsurface.

Estimation of spatial resolution

It is a simplified assumption that the P-wave travels as a ray. It carries information that originates from an integrative volume around the ray path: the Fresnel volume. Based on the work of Jordi et al. (2016) and Watanabe (1999), (Appendix D), we calculate the weighting function for the Fresnel volume using the pyGimli-software (pygimli.org) that offers a range of tools for travel time analysis. We assume our ray propagating through homogeneous saturated sand with $v = 1760$ m/s and 1750 m/s for saturated clay. The gas injection is modeled as a gas-water-saturated area with $v = 1000$ m/s. Due to the loss of high-frequency content from the source to the receivers, we simplify the layout by calculating and comparing the Fresnel volume only with the highest frequency measured during the baseline monitoring ($f = 533$ Hz) and the second monitoring cycle ($f = 466$ Hz) in 10 m depth in homogeneous sand. The models are shown in Figure 6A, B. The circle accounts for the gas-water-saturated area. The red dots indicate the source-receiver points; they model *SB* and *RB2*.

Looking at the travel path at 8 m depth, we see an influence on the Fresnel volume by the low permeable layer, showing that the wave is not taking a straight path

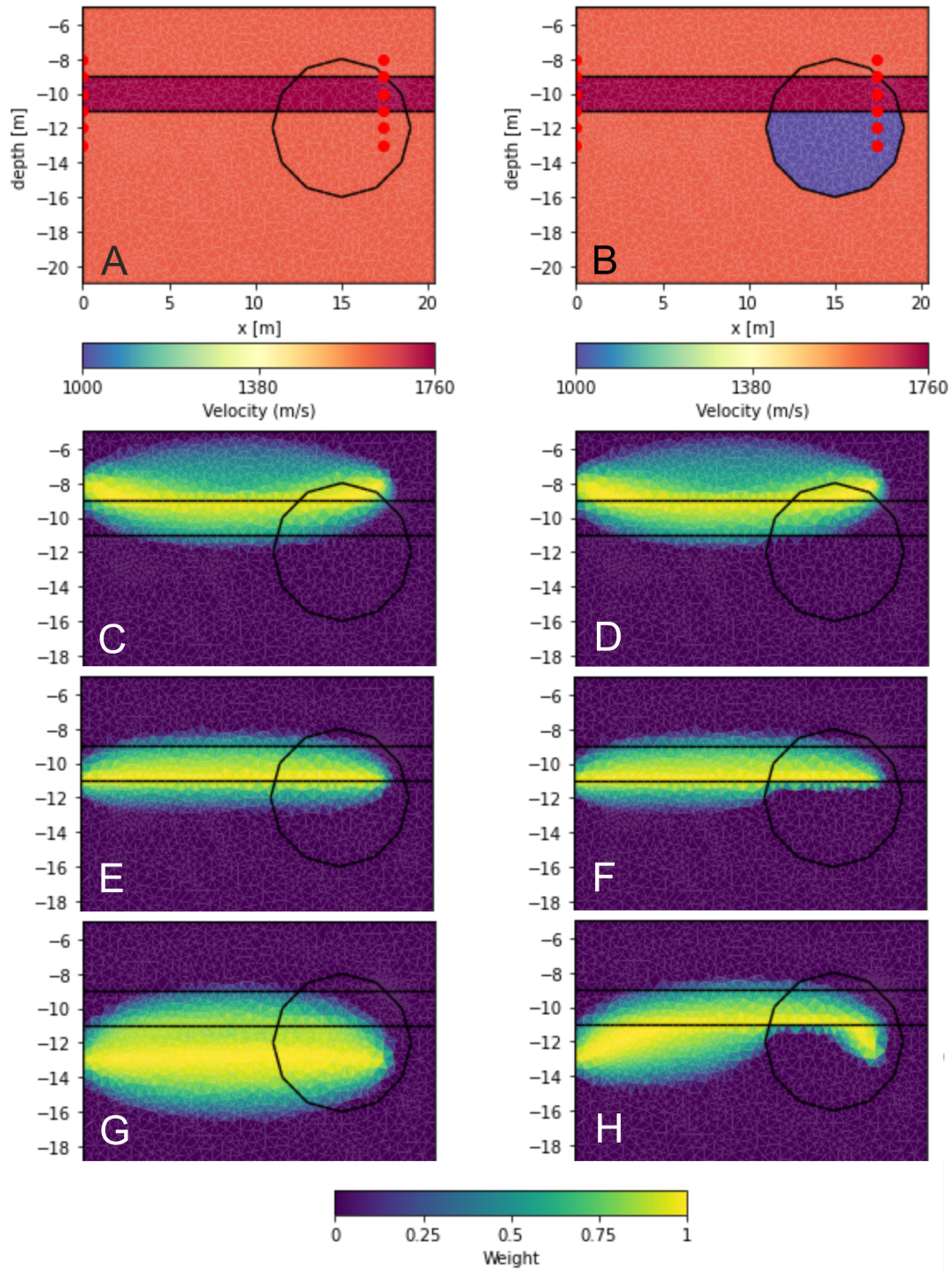


Figure 6: Extent of the Fresnel volume at 8, 11 and 13 m depth. We use a predominant frequency of $f = 533$ Hz for the Baseline model and $f = 466$ Hz for the gas-water-saturated model. A) Model of the baseline condition, B) model of the first monitoring with a gas-water-saturated zone, C) Fresnel volume at 8 m depth with a deviation to the high velocity zone, D) Fresnel volume at 8 m depth with an influence of the gas phase between 10 - 15 m., E) Fresnel volume for a shot at 11 m depth, D) Fresnel volume at 11 m depth with an deviation at the low permeable layer boundary, G) Fresnel volume in the aquifer, H) Fresnel volume with a gas-water-saturated zone. The deviation at the low velocity zone is visible.

(Figure 6C, D). The volume of information influence is somewhat similar compared to the gas-saturated model. The measurement at 11 m depth (Figure 6E, F) shows a narrower extent of the Fresnel volume. The influence is focused along the boundary of the low permeable layer and the sandy aquifer. The gas-water-saturated area already shows an influence. In 13 m depth, we can see the strongest variation between the baseline and the gas-water-saturated model. The volume of influence in the sandy aquifer is higher than in the low permeable layer. The occurrence of a low-velocity area changes the volume of influence into the area with higher P-wave velocities. The volume of influence is decreasing with the occurrence of gas, and we observe a higher smearing in depth without gas. The modeled gas-water-saturation boundaries have thin transition zones that are thicker under real conditions. In conclusion, we have to consider volume information in our experiment. The volume of influence is smaller close to source and receiver and extends to ± 2 m max. in the middle of RB and SB . To account for changes in the subsurface, we have to conduct time-lapse studies and compare monitoring measurements with the baseline measurement. Due to a possible lateral deviation of the layer boundaries, we have to keep in mind that changes can not be transferred directly to a specific depth but work as approximations.

Processing of seismic field data

We perform a time-lapse study and compare all monitoring measurements to a baseline measurement without changing the geology in the background. We detect the P-wave's first arrival in the receiver boreholes (*RB1*, *RB2*) by manual first break picking (FBP) with a picking accuracy of 0.05 ms and obtain the apparent P-wave velocity $v = \frac{\Delta s}{\Delta t}$. Subsequently, we focus our velocity analysis on the area between the receiver boreholes. It is important to analyze these changes between baseline and monitoring measurements since the simulation shows that we can not assume 1D conditions.

Water-content measurements

Water content has been directly measured with soil-moisture sensors (SMT-100, TRUEBNER GmbH) in well D05 and C06 at 11 m and in well Inj2 at 14 m and 18 m depth (Figure 1) with a measurement accuracy of 1% when calibrating soil-specifically (data sheet, TRUEBNER (2021)). The recorded absolute water content can be converted to a volumetric relative gas saturation Θ_{rg} which is calculated by using Θ_{fs} as fully saturated water content and Θ_{mw} as measured water content by Equation 1 where:

$$\Theta_{rg} = \frac{\Theta_{fs} - \Theta_{mw}}{\Theta_{fs}} \quad (1)$$

Rock physical relation

The rock-physical properties are mainly driven by the fluid component and thus are the corresponding geophysical proxies. To obtain gas-induced parameter changes, we

focus on the proxy relationship between our direct geophysical property (velocity) and the indirect property we are interested in (gas content). For unconsolidated material and an environment of homogeneous stress and strain, Reuss (1929) and Voigt (1910) introduce a basic conceptual model. The principle of spatial averaging is based on the separation of individual rock components and their arrangement as a sequence of sheets ("sheet model"). Modifications of the model allow the application of the seismic travel time, such as the time-average relation proposed by Wyllie et al. (1956).

This relationship, also based on the application of the sheet model in porous rocks, is mainly applied to determine or estimate porosities. This assumption is only valid if:

- the wavelength is small compared to the typical pore size
- pores and grains are homogeneously arranged perpendicular to the ray path
- for consolidated materials with intermediate porosity

and, therefore, does not apply for our case. However, Schön (2015) announces the problem of multi-phase pore fluids where the modulus of the mixtures is dominated by the phase with the lowest modulus and, therefore, highest compressibility. If water and gas are evenly distributed in the pore, this results in a jump from bulk modulus of the gas (K_g) level to bulk modulus of water (K_f) level immediately at $S_w \rightarrow 1$. Given that the fluids are not mixed uniformly, he talks of a "patchy saturation" whereupon the Voigt and Reuss equation generally describes the upper and lower limit of the effective moduli, the limit of elastic parameters of a composite medium for any mixture. This allows us to apply the time-average relation (Wyllie et al., 1956) to estimate gas-induced parameter changes independent of subsurface density. It states that the total travelttime recorded on the log is the sum of the time the seismic wave

spends travelling through the solid part of the rock and the time it spends travelling through the fluids in the pores. We obtain the gas content Θ_g by subtracting the traveltimes of the saturated rock before the injection from the traveltimes of the seismic P-wave through the partly saturated rock after the injection.

$$\frac{t_{fs}}{s} = \frac{1}{v_f}\Phi + \frac{1}{v_m}(1 - \Phi) \quad (2)$$

To describe the total traveltimes of the seismic P-wave through the fully saturated rock before the injection. After the gas injection, we receive an additional term with t_{ps} as traveltimes of the partly saturated rock, v_g as the interval velocity of the injected gas and S_w as water saturation.

$$\frac{t_{ps}}{s} = \frac{1}{v_g}\Phi(1 - S_w) + \frac{1}{v_f}\Phi S_w + \frac{1}{v_m}(1 - \Phi) \quad (3)$$

with: s = distance from SB to $RB2$,

t_{fs} = traveltimes of the full saturated rock,

Φ = porosity,

v_m = interval velocity of the matrix material,

v_f = interval velocity of the pore fluid,

s = distance to SB ,

Δt = travel time difference between the fully saturated and the partly saturated rock,

$v_w = 1480$ m/s as the interval velocity of water,

$v_g = 430$ m/s as interval velocity of the injected gas.

When subtracting Equation 2 from Equation 3 we get the traveltime difference between the saturated and the partly saturated subsurface.

$$\frac{\Delta t}{s} = \frac{t_{ps} - t_{fs}}{s} = (1 - S_w)\Phi \left(\frac{1}{v_g} - \frac{1}{v_f} \right) \quad (4)$$

$$\frac{\Delta t}{s} = \Theta_g \left(\frac{1}{v_g} - \frac{1}{v_f} \right) \quad (5)$$

$$\Theta_g = \frac{\frac{\Delta t}{s}}{\frac{1}{v_g} - \frac{1}{v_w}} \quad (6)$$

The calculation of gas content Θ_g using the time-average relationship is based on the picked traveltime difference between *RB1* and *RB2*.

Gassmann (1951) derived a refined relation that is based on the pore fluid effect model and is natural for unconsolidated rock. It applies for saturated porous rocks with any fluid of known properties. Relative motions between fluid and solid are negligible. This results in an inertial density of the saturated rock and hence, justifies the performance only for low frequency ranges from 10-100 Hz (Diallo, 2000; Benson and Wu, 1999). Biot (1956) included dynamic effects through connected pores and allows relative fluid flow resulting in frequency dependence of wave velocity. The low frequency Gassmann (1951)-Biot (1956) theory predicts the relation between the effective bulk moduli of the dry and saturated rock K_{dry} and K_{sat} with the shear

modulus μ being independent on saturation.

$$\frac{K_{sat}}{K_0 - K_{sat}} = \frac{K_{dry}}{K_0 - K_{dry}} + \frac{K_f}{\Phi(K_0 - K_f)} \quad \mu_{sat} = \mu_{dry} \quad (7)$$

where Φ is the porosity, K_0 and K_f are the bulk moduli of the mineral and the fluid material (Mavko et al., 1995). Gassmann's relation is often described as a relation to predict seismic velocities when exchanging the fluid, such as predicting saturated-rock velocities from dry-rock velocities. It is known as the fluid substitution problem (Mavko et al., 2020). The bulk modulus K and the shear modulus μ can be derived from P-wave, and S-wave velocities with:

$$K = \rho(V_p^2 - \frac{4}{3}V_s^2), \quad \mu = \rho V_s^2, \quad \rho = \Phi\rho_f + (1 - \Phi)\rho_0. \quad (8)$$

We face the problem of an unknown shear wave velocity, so the bulk modulus K cannot be extracted. Given that case, Mavko et al. (1995) presented a method to approximate the fluid substitution transform of V_p without knowing V_s by operating directly on the P-wave modulus M .

Applying the fluid substitution problem of Mavko et al. (1995) leads to an analogue equation to Equation 7 for the P-wave modulus, with M_{ps} as the partially saturated P-wave modulus (Equation 9, Equation 10):

$$\frac{M_{sat}}{M_0 - M_{sat}} \approx \frac{M_{dry}}{M_0 - M_{dry}} + \frac{M_f}{\Phi(M_0 - M_f)}, \quad v_{sat} = \sqrt{\frac{M_{sat}}{\rho}} \quad (9)$$

$$\frac{M_{ps}}{M_0 - M_{ps}} \approx \frac{M_{dry}}{M_0 - M_{dry}} + \frac{M_w}{\Phi S_w (M_0 - M_w)} + \frac{M_g}{\Phi (1 - S_w) (M_0 - M_g)} \quad (10)$$

According to them, changes of the bulk modulus are linked to the Reuss (1929) average of the P-wave modulus M_R , as the pore fluid varies and is defined by Equation 11:

$$\frac{1}{M_R} = \frac{\Phi}{M_f} + \frac{1 - \Phi}{M_0} \quad (11)$$

with $M_0 = K_0 + 4/3\mu_0 = \rho V_p^2$ as the mineral- and $M_f = K_f$ as the fluid modulus. In partially saturated rocks at low frequencies, Bachrach and Nur (1998) consider the gas bulk modulus $M_f = M_w + M_g$ as part of the effective modulus of the pore fluid:

$$\frac{1}{M_f} = \frac{S_w}{M_w} + \frac{1 - S_w}{M_g} \quad (12)$$

With known S_w as the water saturation the materials density ρ can be derived in Equation 13 with the combination of ρ_w (density of the fluid) and ρ_g (density of the gas)

$$\rho = \Phi(S_w \rho_w + (1 - S_w) \rho_g) + (1 - \Phi) \rho_0 \quad (13)$$

Bachrach and Nur (1998) introduced a ratio equation for the case of $S_w < 0.9$, with $M_{ps} \approx \text{constant}$. They state that if the residual water saturation at dry conditions can be estimated and average density ρ_1 can be calculated, then the density change

(due to saturation change) $\Delta\rho$ can be extracted using:

$$\rho_1 V_{p1}^2 \approx (\rho_1 + \Delta\rho) V_{p2}^2 \quad (14)$$

with ρ_1 and v_{p1} as the density and the velocity of the unsaturated sand and v_{p2} as the velocity of the fully saturated sand. With the definition of the fluid saturation as depending on fluid content and the porosity of the fluid containing rock, the saturation parameters can be calculated by applying Equation 8 and 13 into the relation Equation 14. The gas content can be derived with $S_g = 1 - S_w$ as the gas saturation and Θ_g as the gas content in Equation 15:

$$S_g = \frac{\Theta_g}{\Phi} = \left(1 + \frac{1 - \Phi}{\Phi} \frac{\rho_0}{\rho_w}\right) \left(\frac{v_1^2}{v_2^2} - 1\right) \quad (15)$$

This approach takes recourse to the conceptual model of Reuss (1929). Using the elastic moduli for data interpretation remains delicate since the pressure dispersion will likely vary during the injection experiment.

RESULTS

We analyzed the repeatability of the experiment and the signal stability in quality over the whole monitoring period displayed in Figure 7. The deviation of the first period maximum amplitude for the first and second measurement cycle amounts to less than 10% for 70% of all the baseline and monitoring measurements. To investigate the influence of a possible borehole deviation on our measurements, the baseline P-wave velocities have been analyzed at *RB1* and *RB2*. (Figure 8A).

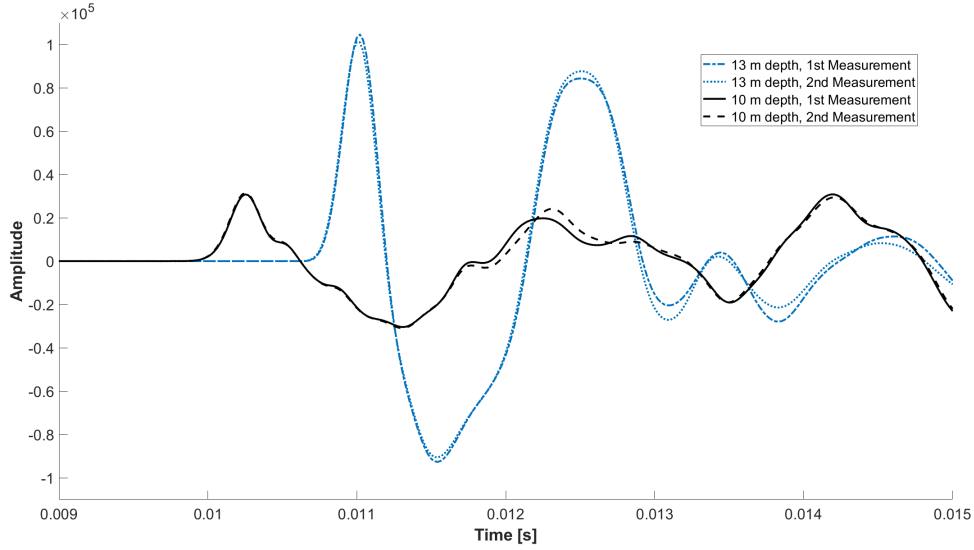


Figure 7: Repeated baseline measurements at 10 and 13 m depth in *RB2*: The first measurement cycle (blue) is followed by a complete dismantle and rebuilt for a second measurement (dotted, dashed).

Traveltime and P-wave velocity data

Figure 8 show the P-wave velocities gathered in the receiver boreholes *RB1* and *RB2*. The traveltime differences between baseline and each monitoring measurement ($dt_B = RB_{\text{Monitoring}} - RB_{\text{Baseline}}$) are displayed in Figure 8B-D for three time steps. Figure 8B shows an increasing traveltime in *RB1* and *RB2* five days after the injection. The strongest shift occurs in *RB2* at 12 m. Two weeks later, the traveltime in both receiver boreholes declines (Figure 8C) so that the traveltime difference becomes negligible 49 days after injection (Figure 8D). Both receiver wells indicate a change in traveltime (Figure 8B-D); thus, we assume the whole area between *RB1* and *RB2* being influenced by gas-induced changes. This allows us to focus our analyses on the area between *RB1* and *RB2*. We derive P-wave velocities from the travel time difference between the receiver boreholes $dt_R = t_{RB2} - t_{RB1}$ (Figure 9). The P-

wave shows strong velocity deviations from the baseline level during the first three monitoring cycles. Follow-up observations from 251 - 355 days after injection indicate smaller to no changes, when seismic P-wave velocity approaches baseline level.

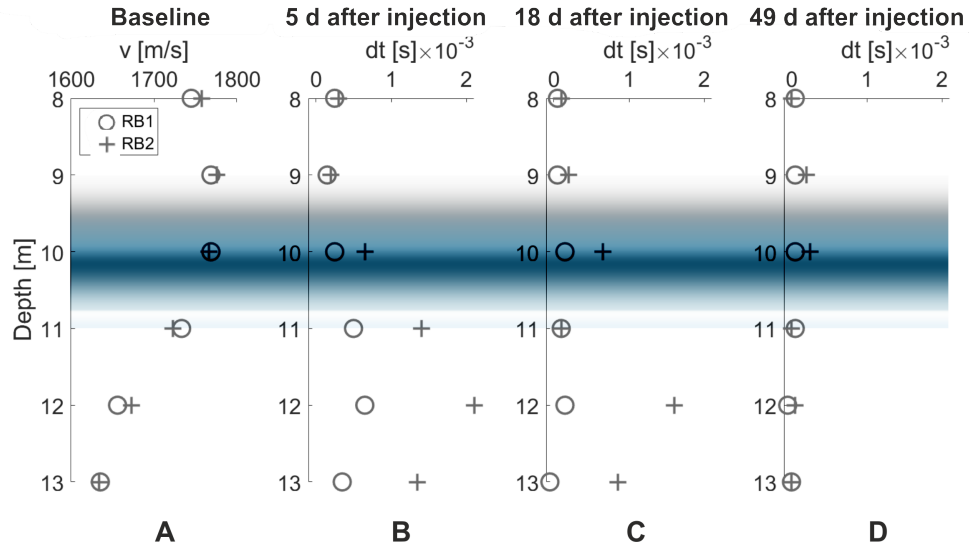


Figure 8: (A) P-wave velocity and (B-D) traveltime difference between baseline and monitoring measurement (dt_B) at different time steps. The blue mark indicates the hydraulic low-permeable layer meandering between 9-11 m depth.

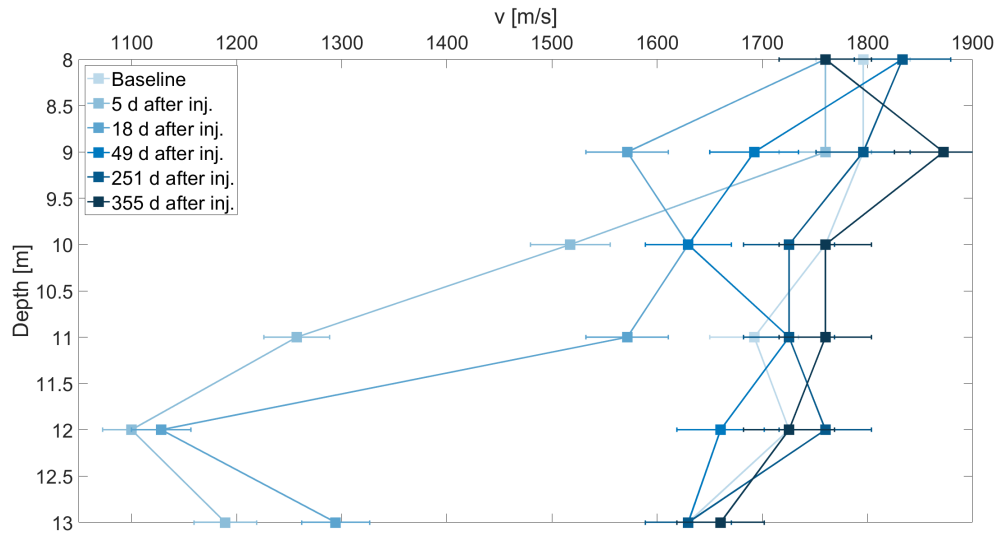


Figure 9: P-wave velocity between the receiver boreholes *RB1* and *RB2* comprising the whole monitoring period

Water content measurements and gas content calculations

Figure 10 provides an overview of water content measurements in well D05 and C06 at 11 m and in Inj2 at 14 m and 18 m depth provides. A direct comparison between P-wave velocities obtained at *RB2* and simultaneous measured water content is given in Figure 10A. Accounted errors are depicted. They comprise the picking accuracy of 2% and the measurement accuracy of the water saturation of 1%. It shows that the measured P-wave velocities are related to water content measured in well D05, C06 and Inj2 during the injection process. Porosity estimates amount to D05 = 36.5%, C06 = 35.5%, Inj2 = 35.1%. Higher water- and, therefore, lower gas content in the subsurface show a higher P-wave velocity between *SB* and *RB2*. Single water content measurements at different boreholes (Figure 10B) show that water content drops stronger in greater depths. Well D05 is situated between *SB* and *RB1*, and water-content information is available at 11 m depth allowing a direct comparison

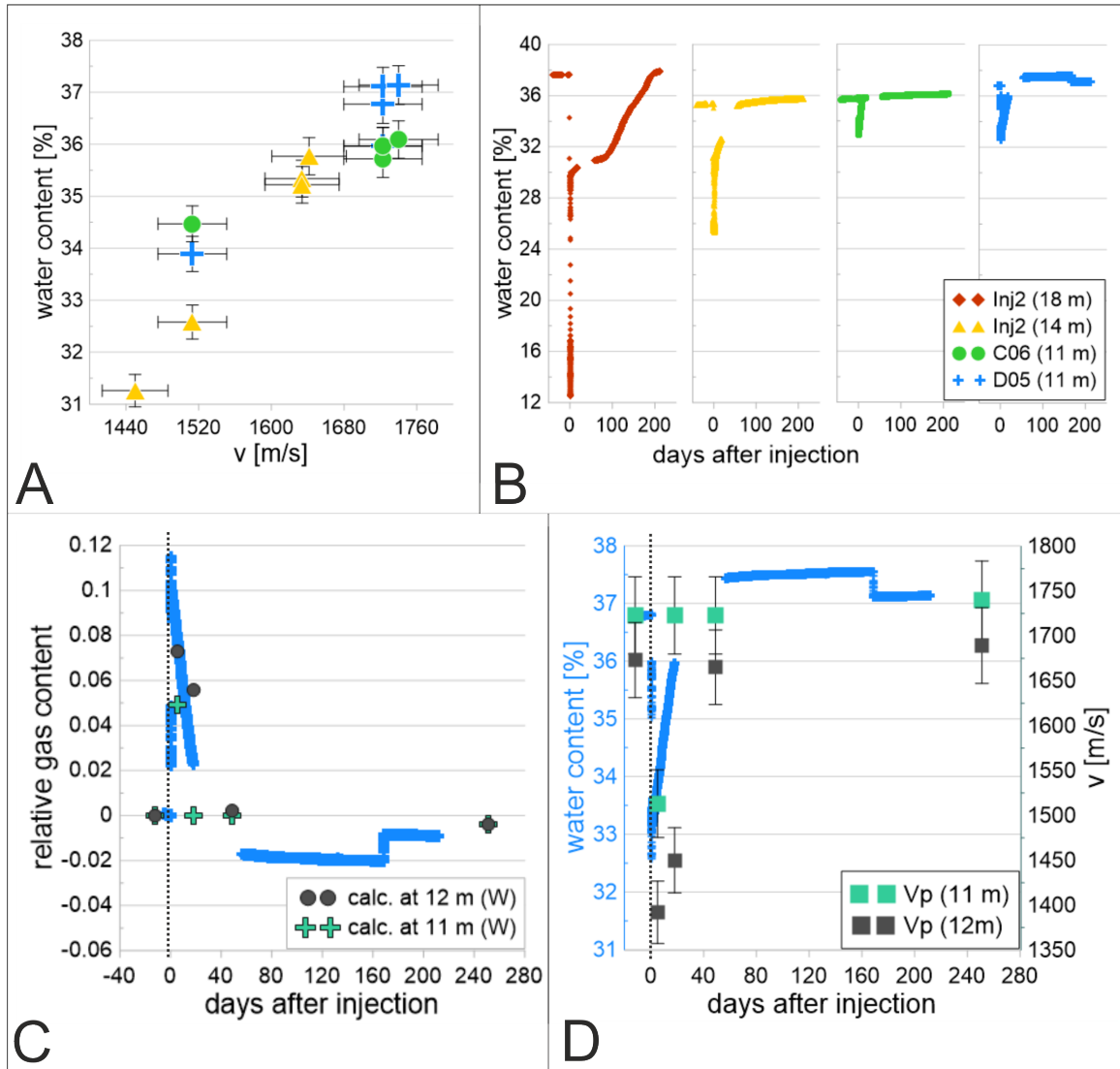


Figure 10: A) Experimentally determined relation between P-wave velocity ($SB-RB2$) and water content B) Soil water at the middle injection well Inj2 at 14 m and 18 m, and at D05 and C06 at 11 m depth, C) calculated gas content values based on the time average relation (Equation 6) plotted against collected gas content values, D) Water content at D05 at a sensor in 11 m depth, P-wave velocity at 11 and 12 m depth at $RB2$. Injection timing is indicated by the dashed line.

with the P-wave velocity. The calculation of the gas content using the experimentally determined parameters in *RB2* and its comparison to the measured value delivered the following results in Table 3. They are visually apparent in Figure 10C. The gas content graph of D05 clearly rises directly after injection. The calculated gas content inferred from the time average relation (Equation 6) shows an increase around the injection time. The calculated gas content culminates in 7.3% at 12m depth five days after injection. Those calculated values using the seismic data (Equation 6) in Table 3 show the absolute change in gas content Θ_g in *RB2* with a defined error margin of 0.2 Vol.% due to picking accuracy of 0.05 ms. Physically a gas content of -0.4 Vol.% is not reasonable but indicates our measurement accuracy. Gas content is 0 when the subsurface reaches the initial condition. The increase in gas corresponds to a maximum drop of 4.2% in water content (Figure 10D). The measured P-wave velocity at 11 and 12m depth show a drop around the injection time. In our initial seismic measurement at *RB2* we record a drop in P-wave velocity of 209 m/s five days after the injection compared to our baseline measurement. In Figure 10D the actual measured water content is plotted together with the measured P-wave velocity in *RB2* at 11 and 12 m depth.

Table 3: Gas content Θ_g in [Vol.%] for each depth calculated for four time steps after injection according to Equation 6.

Depth [m]	5 days after inj.	18 days after inj.	49 days after inj.	251 days after inj.
13	4.7	3	0	0
12	7.3	5.6	0.2	-0.4
11	4.9	0	0	-0.4
10	2.3	2.3	0.9	0.2
9	0.7	0.7	0.7	0
8	1	0.4	0	0

The results and corresponding parameters of the Gassmann evaluation according to Bachrach and Nur (1998) using Equation 15 is provided in Appendix C, Table 5.

DISCUSSION

Similar to Lamert et al. (2012, measuring CO_2 with ERT) and Cahill et al. (2017, measuring CH_4 with GPR), we injected methane into the near surface to detect gas-induced parameter changes with geophysical methods. Our new approach of implementing a seismic crosshole set-up analogous to Diallo (2000) closed a gap in near-surface monitoring approaches.

With our re-measurement procedure, we excluded errors due to manually handled equipment (Figure 7) and ensured the approach by comparing data sets of different time steps. We thereafter quantify gas saturation by evaluating P-wave velocities and hence, connect established rock physics theories with hydrogeophysical applications.

Borehole deviation and traveltimes

Similar P-wave velocities for both receiver boreholes in Figure 8A signify the negligible effect of borehole deviation on our measurement. The time series of traveltimes displayed in Figure 8B, C shows a shift between the first and the second receiver borehole, strongest at 12 m depth. After 49 days after the injection, the traveltimes in both receiver boreholes re-approach the baseline level. With this shift and the hydraulic low-permeable layer being situated between 9-11 m depth, we assume that gas accumulates beneath the silt layer.

P-wave velocity

Initially conducted elastic wavefield simulations show the feasibility of P-waves to detect saturation changes in the subsurface. Depending on the sources location towards

the layer boundaries, we observe reflection, refraction and conversion processes. The first break pick detects a non-converted P-wave. The alteration of P-wave velocity and associated changes in gas content between *RB1* and *RB2* are strongest within the first two months after injection at a depth of 10-13 m (Figure 9). At a depth of 9-10 m, the velocity remains lower compared to the baseline 49 days after injection. With glacial till having a much smaller permeability than silty sand (Schön (2004)), this could be due to a slower process of degassing and dissolving or an upwards gas migration. With the last monitoring cycle 355 days after injection, we found no gas indication in the velocity analysis and, therefore, assumed a complete dissolving of the gas.

Comparison to in-situ soil-water content

The verification of seismic data with the absolute water content in the soil, also done by Whiteley et al. (2020) when investigating landslides using seismic refraction tomography, has been applied here on smaller-scale studies in a borehole setup. The effect of the soil-water content on seismic reflection and refraction amplitude has already been studied by Jefferson et al. (1998). Here, we compared the water content and calculated gas content Θ_g primarily with the observed P-wave velocities between *RB1* and *RB2* (Figure 10). With the injection taking place at 17.5 m depth, we see a strong reaction at the soil-moisture sensors in greater depths directly at the injection lance. The response of the more distant soil moisture sensors at C06 and D05 at 11 m depths is much weaker (Figure 10B). The correlation of water content and P-wave velocity shows that higher gas content corresponds to lower P-wave velocities

(Figure 10A). The "patchy saturation" approach allows us to simplify our calculations using the time-average relation. We have a detailed look at the soil moisture sensor at D05 in 11 m depth and compare it to the P-wave velocity measurements at 11 m depth. The instant drop of water content by 4.2% seems to be reflected by the calculated P-wave velocity which was obtained five days after the injection, where we see a drop of 209 m/s. The accurate water content five days after the injection amounts only to 34.2% at the water-content measuring well D05. Gas propagation simulations (Dahmke et al., 2021) assume that the influence of the gas phase does not exceed a lateral extent of 2 m radius around the injection point and, therefore, still includes D05, but not *RB1*. A direct comparison between water content and seismic P-wave velocity is still valid when we consider that the seismic P-wave transports 2D information on the path between the source and the receiver. The monitoring interval should be increased around the injection period for higher accuracy. The translation of the water content to a relative gas content allows a direct comparison of the gas saturation changes (Figure 10B). The correlation of water content and P-wave velocity shows that higher gas content corresponds to lower P-wave velocities (Figure 10C). The calculated Θ_g in Table 3 of 4.9% at 11 m depth five days after injection complies well with our P-wave velocity data, the relative gas content and the water content measurements. When we compare the calculated percent deviation with the absolute deviation, we find a very good correlation that shows our seismic crosshole measurement's capability to indicate and quantify relative gas content changes in the subsurface. Figure 10 shows the compliance of these three parameters and their following increase beyond the baseline level at the end of the monitoring

process.

Analyzing the approach of Mavko et al. (1995) of inferring K without knowing the S-wave velocity (Table 5) shows rather high gas contents. Those calculations consider density properties in the subsurface. Changes in density can not be evaluated and reconsidered during the experiment; thus we cannot provide realistic density assumptions. Therefore, this gas content estimation is not fully parameterizable.

The whole signal, whilst repetitive and resilient, underlies a complex behavior in the subsurface. A full-waveform analysis of this data set would be of great interest, also for tackling potential frequency dependencies, but must handle high frequencies and the elastic approximation in order to image the low variations of the time-series application (Köhn et al., 2013, 2017). Another approach would be the analysis of S-wave behavior which would require different well sizes and borehole equipment. This basic field experiment shows the urgent need for further and continuative investigations of rock-physical dependencies at the field scale.

CONCLUSION

With our crosshole seismic experiment in the near surface we are able to detect gas-induced changes in matrix saturation at the field scale. Seismic monitoring before and after methane injection provided comparable time series of P-wave traveltime, and velocity. With this new approach, we generate highly repeatable data when monitoring the impact of gas injection during a time period of twelve months. We developed a ready-to-apply field approach to identify gas leakages in the near surface using three boreholes equipped with one sparker and two hydrophone chains. The experimen-

tal design is suitable to monitor gas-induced changes reflected by seismic velocity at the field scale. The P-wave velocities have been compared to absolute water content measurements as well as to calculated gas content values. We discussed different approaches on quantifying gas content changes by comparing Gassmann's equations and the time-average relation. With the idea of "patchy saturation", we discovered a suitable method for our experiment with a measurement accuracy of 0.2 Vol. % in the subsurface by analyzing seismic P-wave velocities. Additional favorable approaches to analyze the behavior of seismic waves in combination with saturation changes would imply focus on complementing processing approaches such as, frequency and dispersion analysis and provide real data for full waveform analysis. Acquiring shear waves is essential to support and confirm further theoretical concepts. In the future, gaining substantial knowledge about parameter relation and dependencies in the near surface entails a huge potential considering the small number of field scale experiments.

APPENDIX A

RESORTED CROSSHOLE DATA

Resorted data that accounts for horizontal transmission. The Figure A-1 shows eight traces at each depth per measurement. The colors indicates similar measurement periods.

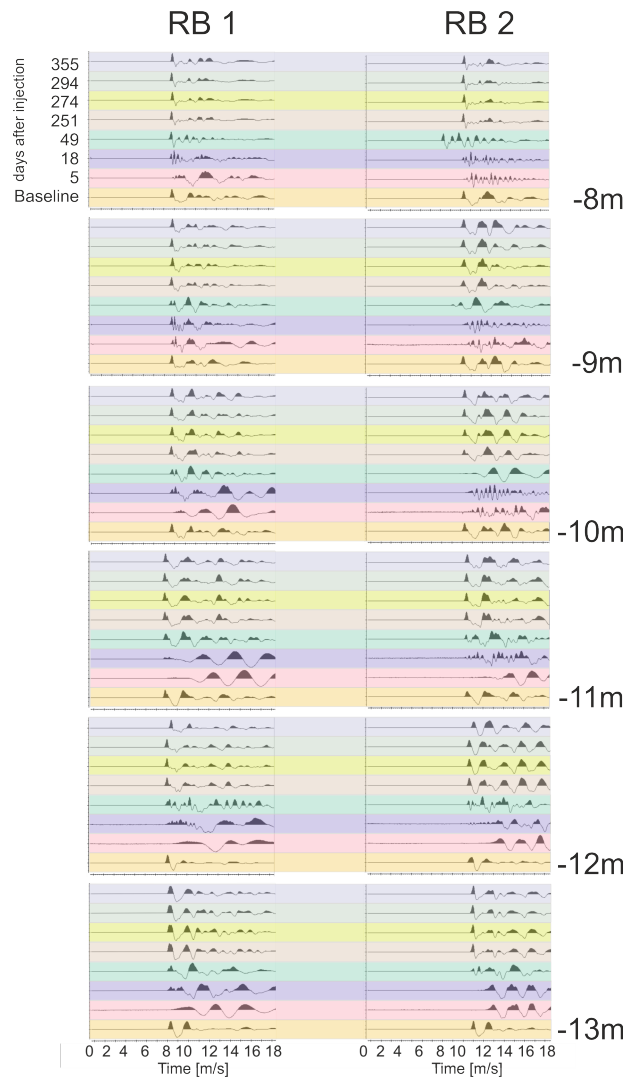


Figure A-1: Crosshole traces for every measurement sorted by depth. Different colors indicate similar measurement periods.

APPENDIX B**SOURCE SIGNAL SIGNATURE**

The source signal signature is described by a Ricker wavelet with the dominant frequency of 4.3kHz.

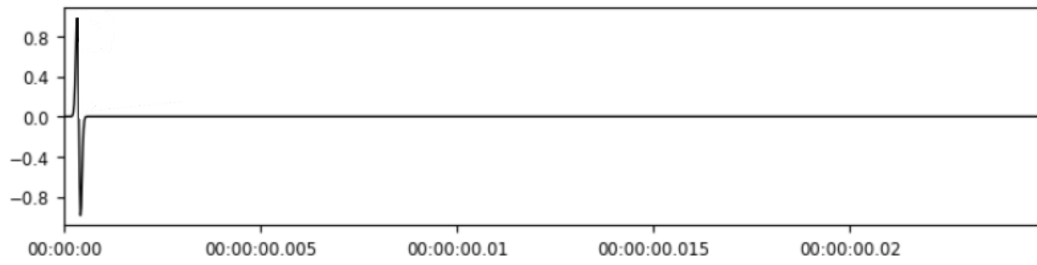


Figure B-1: Ricker wavelet

APPENDIX C

**GAS CONTENT APPLYING THE APPROXIMATION METHOD
AFTER MAVKO ET AL. (1995) AND BACHRACH AND NUR (1998)**

Mavko et al. (1995) provided a method, using the Reuss (1929) average to estimate the K- modulus without knowing the S-wave velocity and, therefore, the shear modulus.

With:

Φ = Porosity

M_R = Reuss average modulus

$M_0 = K_0 + 4/3\mu_0$ = mineral modulus

$M_f = K_f$ = fluid modulus

$M_g = K_g$ = gas modulus

The calculation of the gas content following Mavko et al. (1995) and Bachrach and Nur (1998) has been performed using the following parameters:

Table 4: Parameters for calculating P-wave velocity depending on water saturation according to Mavko et al. (1995); Bachrach and Nur (1998)

Parameter	Symbol	Value	Unit
Bulk density	ρ	1500 - 1800	kg x m ⁻³
Density Water	ρ_f	999	kg x m ⁻³
Density Methan	ρ_g	0.717	kg x m ⁻³
P-wave velocity water	V_{pf}	1480	m x s ⁻¹
P-wave velocity methane	V_{pg}	430	m x s ⁻¹

Table 5: Gas content Θ_g in [Vol.-%] for each depth calculated for four time steps after injection following Bachrach and Nur (1998).

Depth [m]	5 days after inj.	18 days after inj.	49 days after inj.	251 days after inj.
13	55	33	-	-
12	90	67	2	-4
11	60	-	-	-4
10	27	27	1	-2
9	8	8	8	-
8	12	4	-	-

APPENDIX D

FRESNEL VOLUME CALCULATION

The Fresnel volume indicates the integrative area of the amplitude measurement. It is calculated by using:

T_S = Traveltime from SB

T_G = Traveltime from $RB1$ to each grid point P in the area of interest.

T_{SR} = traveltime from SB to $RB1$

x = horizontal position of source- and receiver point (here: 0 m, 13 m)

z = lateral position of source- and receiver point (here: -10 m)

f = dominant frequency

The Fresnel volume is represented as weight value w that are expressed as a monotonously decreasing function:

$$TS = \frac{\sqrt{(x_{SB})^2 + (z_{SB})^2}}{v} \quad (\text{D-1})$$

$$TG = \frac{\sqrt{(x_{RB1})^2 + (z_{RB1})^2}}{v} \quad (\text{D-2})$$

$$T_{SP} + T_{PR} - T_{SR} \leq \frac{1}{2f} \quad (\text{D-3})$$

Here, according to Watanabe (1999), as a linear weighting function:

$$w = \begin{cases} 1 - 2f\Delta t, & (0 \leq \Delta t \leq 1/2f) \\ 0, & (1/2f \leq \Delta t) \end{cases} \quad (\text{D-4})$$

with

$$\Delta t = T_{SP} + T_{PR} - T_{SR} \quad (\text{D-5})$$

APPENDIX E

DATA SET AVAILABILTY AND TEST SITE LABELING

The original data used for this paper will be provided in Pangaea (Pohle et al., 2022):

<https://doi.org/10.1594/PANGAEA.940676>

Label	Test Site	Purpose
Inj1	<i>W3_ML_C03</i>	Gas injection
Inj2	<i>W3_ML_C04</i>	Gas injection
Inj3	<i>W3_ML_C05</i>	Gas injection
RB1	<i>W3_2Z_U05</i>	Receiver borehole 1
RB2	<i>W3_2Z_D06</i>	Receiver borehole 2
SB	<i>W3_2Z_U00</i>	Source borehole
MP028	<i>WZ_2Z_006</i>	HPT / Core
MP031	MP031	HPT
MP032	MP032	HPT
D05	<i>W3_ML_D05</i>	Water content

REFERENCES

- Allen, N. F., F. E. Richart Jr, and R. D. Woods, 1980, Fluid wave propagation in saturated and nearly saturated sands: *Journal of Geotechnical and Geoenvironmental Engineering*, **106**, 235–254.
- Bachrach, R., and A. Nur, 1998, High-resolution shallow-seismic experiments in sand, part i: Water table, fluid flow, and saturation: *GEOPHYSICS*, **63**, 1225–1233.
- Benson, A. K., and J. Wu, 1999, A modeling solution for predicting (a) dry rock bulk modulus, rigidity modulus and (b) seismic velocities and reflection coefficients in porous, fluid-filled rocks with applications to laboratory rock samples and well logs: *Journal of Applied Geophysics*, **41**, 49–73.
- Binley, A., S. S. Hubbard, J. A. Huisman, A. Revil, D. A. Robinson, K. Singha, and L. D. Slater, 2015, The emergence of hydrogeophysics for improved understanding of subsurface processes over multiple scales: *Water Resources Research*, **51**, 3837–3866.
- Biot, M. A., 1956, Theory of propagation of elastic waves in a fluid-saturated porous solid. i. low-frequency range: *The Journal of the Acoustical Society of America*, **28**, 168–178.
- Blazevic, L., L. Bodet, S. Pasquet, N. Linde, D. Jougnot, and L. Longuevergne, 2020, Time-lapse seismic and electrical monitoring of the vadose zone during a controlled infiltration experiment at the ploemur hydrological observatory, France: *Water*, **12**.
- Butler, J. J., 1997, *The design, performance, and analysis of slug tests*: CRC Press.
- Cahill, A. G., C. M. Steelman, O. Forde, O. Kuloyo, S. Emil Ruff, B. Mayer, K.

- Ulrich Mayer, M. Strous, M. Cathryn Ryan, J. A. Cherry, and B. L. Parker, 2017, Mobility and persistence of methane in groundwater in a controlled-release field experiment: *Nature Geoscience*, **10**, 289–294.
- Dahmke, A., G. Hornbruch, K. Lüders, S. Bauer, L. Hu, P. Dietrich, U. Werban, S. Birnstengel, H.-H. Richnow, N.-S. Keller, H. Geistlinger, and B. Zulfiqar, 2021, Verbundprojekt UG: TestUM-Aquifer - Testfeld zur Untersuchung und zum Monitoring durch die Nutzung des Untergrundes induzierter reaktiver Mehrphasentransportprozesse in oberflächennahen Aquiferen: Abschlussbericht 03G0875A/B.
- Dangeard, M., A. Rivière, L. Bodet, S. Schneider, R. Guérin, D. Jougnot, and A. Maineult, 2021, River corridor model constrained by time-lapse seismic acquisition: *Water Resources Research*, **57**.
- Diallo, M. S., 2000, Acoustic waves attenuation and velocity dispersion in fluid-filled porous media: theoretical and experimental investigations: *Tübinger Geowissenschaftliche Arbeiten (TGA) : Reihe C, Hydro-, Ingenieur- und Umweltgeologie*.
- Dietrich, P., J. J. Butler Jr, and K. Faiß, 2008, A rapid method for hydraulic profiling in unconsolidated formations: *Groundwater*, **46**, 323–328.
- Dietrich, P., and C. Leven, 2006, *in* *Groundwater Geophysics: A Tool for Hydrogeology*: Springer Berlin Heidelberg, 321–340.
- Dietrich, P., and J. Tronicke, 2009, Integrated analysis and interpretation of cross-hole P- and S-wave tomograms: a case study: *Near Surface Geophysics*, **7**, 101–109.
- Dlugosch, R., 2014, Aquifer characterisation using nuclear magnetic resonance: Doctoral thesis, Technische Universität Berlin, Fakultät VI - Planen Bauen Umwelt, Berlin.

- Gassmann, F., 1951, Über die Elastizität poröser Medien: Vierteljahrsschrift der Naturforschenden Gesellschaft in Zürich, **96**, 1–23.
- Geistlinger, H., and B. Zulfiqar, 2020, The impact of wettability and surface roughness on fluid displacement and capillary trapping in 2-D and 3-D porous media: 1. Wettability-controlled phase transition of trapping efficiency in glass beads packs: Water Resources Research, **56**, e2019WR026826.
- Geotomographie, 2021, Datasheet SBS 42 — P-Wave Source.
- Götz, J., 2014, Borehole seismic monitoring of CO₂ storage within a saline aquifer at ketzin, germany: Doctoral thesis, Technische Universität Berlin, Fakultät VI - Planen Bauen Umwelt, Berlin.
- Hausmann, J., H. Steinel, M. Kreck, U. Werban, T. Vienken, and P. Dietrich, 2013, Two-dimensional geomorphological characterization of a filled abandoned meander using geophysical methods and soil sampling: Geomorphology, **201**, 335–343.
- Heldt, S., B. Wang, L. Hu, G. Hornbruch, K. Lüders, U. Werban, and S. Bauer, 2021, Numerical investigation of a high temperature heat injection test: Journal of Hydrology, **597**, 126229.
- Hellwig, O., 2017, A seismic exploration ahead of boreholes using borehole-guided waves: A feasibility study.: Doctoral thesis, Technische Universität Freiberg, Fakultät für Geowissenschaften, Geotechnik und Bergbau, Freiberg.
- Hing Ng, Y. C., W. Danovan, and T. Ku, 2019, The potential of seismic cross-hole tomography for geotechnical site investigation: E3S Web Conf., **92**, 18006.
- Hu, L., J. Doetsch, R. Brauchler, and P. Bayer, 2017, Characterizing CO₂ plumes in deep saline formations: Comparison and joint evaluation of time-lapse pressure

- and seismic tomography: *Geophysics*, **82**, 1–70.
- Jefferson, R. D., D. W. Steeples, R. A. Black, and T. Carr, 1998, Effects of soil-moisture content on shallow-seismic data: *GEOPHYSICS*, **63**, 1357–1362.
- Jordi, C., C. Schmelzbach, and S. Greenhalgh, 2016, Frequency-dependent travelttime tomography using fat rays: application to near-surface seismic imaging: *Journal of Applied Geophysics*, **131**, 202–213.
- Jorgensen, D. G., 1989, Using geophysical logs to estimate porosity, water resistivity and intrinsic permeability: Report 2321.
- Keller, N.-S., G. Hornbruch, K. Lüders, U. Werban, C. Vogt, R. Kallies, A. Dahmke, and H. H. Richnow, 2021, Monitoring of the effects of a temporally limited heat stress on microbial communities in a shallow aquifer: *Science of The Total Environment*, **781**, 146377.
- Köber, R., G. Hornbruch, C. Leven, L. Tischer, J. Grossmann, P. Dietrich, H. Weiss, and A. Dahmke, 2009, Evaluation of combined direct-push methods used for aquifer model generation: *Ground water*, **47**, 536–46.
- Köhn, D., S. Al Hagrey, and W. Rabbel, 2013, Monitoring of underground gas storage sites by elastic 2D time-lapse waveform inversion.
- Köhn, D., D. De Nil, M. Thorwart, W. Rabbel, C. Hübscher, and W. Pfeiffer, 2017, Überwachung unterirdischer Energiespeicher und Kartierung potentieller Leckagepfade mit seismischer Full Waveform Inversion: Presented at the ANGUS Symposium 2017: Energiespeicher im geologischen Untergrund. ANGUS, Kiel.
- Lamert, H., H. Geistlinger, U. Werban, C. Schütze, A. Peter, G. Hornbruch, A. Schulz, M. Pohlert, S. Kalia, M. Beyer, J. Großmann, A. Dahmke, and P. Dietrich,

- 2012, Feasibility of geoelectrical monitoring and multiphase modeling for process understanding of gaseous CO₂ injection into a shallow aquifer: *Environmental Earth Sciences*, **67**, 447–462.
- Lumley, D., D. Adams, R. Wright, D. Markus, and S. Cole, 2008, *in* Seismic monitoring of CO₂ geo-sequestration: Realistic capabilities and limitations: Society of Exploration Geophysicists, SEG Technical Program Expanded Abstracts, 2841–2845.
- Lüders, K., G. Hornbruch, N. Zarrabi, S. Heldt, A. Dahmke, and R. Köber, 2021, Predictability of initial hydrogeochemical effects induced by short-term infiltration of 75 °C hot water into a shallow glaciogenic aquifer: *Water Research X*, **13**, 100121.
- Mavko, G., C. Y. Chan, and T. Mukerji, 1995, Fluid substitution: Estimating changes in vp without knowing vs: *Geophysics*, **60**, 1750–1755.
- Mavko, G., T. Mukerji, and J. Dvorkin, 2020, *The rock physics handbook*, 3 ed.: Cambridge University Press.
- Meister, E., 2012, *Grundpraktikum physikalische Chemie: Theorie und Experimente*, 2 ed.: vdf Hochschulverlag AG an der ETH Zürich.
- Nanda, N. C., 2016, *Seismic data interpretation and evaluation for hydrocarbon exploration and production*: Springer International.
- Onishi, K., T. Ueyama, T. Matsuoka, D. Nobuoka, H. Saito, H. Azuma, and Z. Xue, 2009, Application of crosswell seismic tomography using difference analysis with data normalization to monitor CO₂ flooding in an aquifer: *International Journal of Greenhouse Gas Control*, **3**, 311–321.
- Paasche, H., U. Werban, and P. Dietrich, 2009, Near-surface seismic traveltimes to-

- mography using a direct-push source and surface-planted geophones: *Geophysics*, **74**.
- Peter, A., H. Lamert, M. Beyer, G. Hornbruch, B. Heinrich, A. Schulz, H. Geistlinger, B. Schreiber, P. Dietrich, U. Werban, C. Vogt, H.-H. Richnow, J. Großmann, and A. Dahmke, 2012, Investigation of the geochemical impact of CO₂ on shallow groundwater: design and implementation of a CO₂ injection test in northeast germany: *Environmental Earth Sciences*, **67**, 335–349.
- Pevzner, R., 2020, *in* Chapter 6.1 - Active surface and borehole seismic monitoring of a small supercritical CO₂ injection into the subsurface: experience from the CO₂CRC Otway Project: Elsevier, 497–522.
- Pohle, M., S. Birnstengel, H. Kotas, K. Peisker, A. Schoßland, J. Schultz, and U. Werban, 2022, Seismic crosshole data at the TestUM site in Wittstock/Dosse (Germany): PANGAEA.
- Randall, C., D. J. Scheibner, and P. T. Wu, 1991, Multipole borehole acoustic waveforms: Synthetic logs with beds and borehole washouts: *Geophysics*, **56**, 1757–1769.
- Reuss, A., 1929, Berechnung der Fließgrenze von Mischkristallen aufgrund der Plastizitätsbedingung für Einkristalle.: *ZAMM - Journal of Applied Mathematics and Mechanics / Zeitschrift für Angewandte Mathematik und Mechanik*, **9**, 49–58.
- Robinson, D. A., A. Binley, N. Crook, F. D. Day-Lewis, T. P. A. Ferré, V. J. S. Grauch, R. Knight, M. Knoll, V. Lakshmi, R. Miller, J. Nyquist, L. Pellerin, K. Singha, and L. Slater, 2008, Advancing process-based watershed hydrological research using near-surface geophysics: a vision for, and review of, electrical and magnetic geophysical methods: *Hydrological Processes*, **22**, 3604–3635.

- Romero-Ruiz, A., N. Linde, L. Baron, S. G. Solazzi, T. Keller, and D. Or, 2021, Seismic signatures reveal persistence of soil compaction: *Vadose Zone Journal*, **20**.
- Schulze-Makuch, D., D. A. Carlson, D. S. Cherkauer, and P. Malik, 1999, Scale dependency of hydraulic conductivity in heterogeneous media: *Groundwater*, **37**, 904–919.
- Schön, J. H., 2004, *Physical properties of rocks: Fundamentals and principles of petrophysics*: Elsevier, **18**.
- , 2015, *Physical properties of rocks: Fundamentals and principles of petrophysics*: Elsevier, **2**.
- Solazzi, S. G., J. Hunziker, E. Caspari, J. G. Rubino, M. Favino, and K. Holliger, 2020, Seismic signatures of fractured porous rocks: The partially saturated case: *Journal of Geophysical Research: Solid Earth*, **125**.
- Trautz, R., 2020, Geophysical monitoring using active seismic techniques at the Citronelle Alabama CO₂ storage demonstration site: *International Journal of Greenhouse Gas Control*, **99**, 103084.
- TRUEBNER, 2021, Datasheet SMT100.
- Voigt, W., 1910, *Lehrbuch der Kristallphysik: (mit Ausschluss der Kristalloptik)*: BG Teubner, **34**.
- Watanabe, T., 1999, Seismic travelttime tomography using Fresnel volume approach: *Seg Technical Program Expanded Abstracts*, **18**.
- Whiteley, J., J. Chambers, S. Uhlemann, J. Boyd, M. Cimpoiasu, J. Holmes, C. Inauen, A. Watlet, L. Hawley-Sibbett, C. Sujitapan, R. Swift, and J. Kendall, 2020, Landslide monitoring using seismic refraction tomography – the importance

- of incorporating topographic variations: *Engineering Geology*, **268**, 105525.
- Wightman, W. E., F. Jalinoos, P. Sirles, and K. Hanna, 2004, Application of geophysical methods to highway related problems.: Report 200512.
- Wyllie, M. R. J., A. R. Gregory, and L. W. Gardner, 1956, Elastic wave velocities in heterogeneous and porous media: *Geophysics*, **21**, 41–70.
- Zhang, F., C. Juhlin, C. Cosma, A. Tryggvason, and R. G. Pratt, 2012, Cross-well seismic waveform tomography for monitoring CO₂ injection: a case study from the Ketzin Site, Germany: *Geophysical Journal International*, **189**, 629–646.

LIST OF FIGURES

1 (A) Location of test site for CH_4 injection and (B) Experimental layout for CH_4 injection with different types of measuring wells. (C) Three hydraulic (black) and electrical conductivity (red) profiles at $MP32$, $MP31$, $MP28$ measured with the Hydraulic Profiling Tool (HPT) and (D) core profile of $MP28$ from 8-16 m depth.

2 Three HDPE wells (CMT-System, Solinst) are installed inline. The P-wave sparker in SB operates at a depth from 13 to 8 m depth. The hydrophone strings in $RB1$ and $RB2$ cover the same depth range. The groundwater table is located at 3 m depth. The gas is injected between $RB1$ and $RB2$ at a depth of 17.5 m via three injection lances. The injection model shows a possible saturation dispersion scenario with the highest gas phase saturation accumulating beneath the low permeable loam.

3 Overview of the applied model parameters. At 2.5 m - 3.0 m depth the transition zone marks the groundwater table represented by linear saturation interpolation. The solid line marks the fully water saturated case, the dashed line marks the gas-water saturated case. A radial gas concentration decrease is implemented to 5 m lateral extend, center at $x = 14.5$ m and $z = 12$ m depth with maximum gas concentration.

4 Simulated P-wave travel path for shot at 8 m depth without gas (left) and with gas lens center at $x = 14.5$ m and $z = 12$ m depth (right)

5 Simulated P-wave travel path for shot at 13 m depth without gas (left) and with gas lens center at $x = 14.5$ m and $z = 12$ m depth (right)

6 Extent of the Fresnel volume at 8, 11 and 13 m depth. We use a predominant frequency of $f = 533$ Hz for the Baseline model and $f = 466$ Hz for the gas-water-

saturated model. A) Model of the baseline condition, B) model of the first monitoring with a gas-water-saturated zone, C) Fresnel volume at 8 m depth with a deviation to the high velocity zone, D) Fresnel volume at 8 m depth with an influence of the gas phase between 10 - 15 m., E) Fresnel volume for a shot at 11 m depth, D) Fresnel volume at 11 m depth with a deviation at the low permeable layer boundary, G) Fresnel volume in the aquifer, H) Fresnel volume with a gas-water-saturated zone. The deviation at the low velocity zone is visible.

7 Repeated baseline measurements at 10 and 13 m depth in *RB2*: The first measurement cycle (blue) is followed by a complete dismantle and rebuilt for a second measurement (dotted, dashed).

8 (A) P-wave velocity and (B-D) traveltime difference between baseline and monitoring measurement (dt_B) at different time steps. The blue mark indicates the hydraulic low-permeable layer meandering between 9- 11 m depth.

9 P-wave velocity between the receiver boreholes *RB1* and *RB2* comprising the whole monitoring period

10 A) Experimentally determined relation between P-wave velocity (*SB-RB2*) and water content B) Soil water at the middle injection well Inj2 at 14 m and 18 m, and at D05 and C06 at 11 m depth, C) calculated gas content values based on the time average relation (Equation 6) plotted against collected gas content values, D) Water content at D05 at a sensor in 11 m depth, P-wave velocity at 11 and 12 m depth at *RB2*. Injection timing is indicated by the dashed line.

A-1 Crosshole traces for every measurement sorted by depth. Different colors indicate similar measurement periods.

B-1 Ricker wavelet

LIST OF TABLES

- 1 Monitoring period
- 2 Model dimension. Source pressure rate is first deviation after time of a bell curve with the main frequency of 4.8 kHz.
- 3 Gas content Θ_g in [Vol.%] for each depth calculated for four time steps after injection according to Equation 6.
- 4 Parameters for calculating P-wave velocity depending on water saturation according to Mavko et al. (1995); Bachrach and Nur (1998)
- 5 Gas content Θ_g in [Vol.%] for each depth calculated for four time steps after injection following Bachrach and Nur (1998).
- 6 Test Site Labeling